Asymmetry-enhanced performance in bistable energy harvesters: An experimental study

João Pedro Norenberg[a,*], Paulo S. Varoto[b], Samuel da Silva[a], Americo Cunha Jr[c,d]

[a] *Universidade Estadual Paulista – UNESP, Ilha Solteira, Brazil*
[b] *University of São Paulo – USP, São Carlos, Brazil*
[c] *National Laboratory of Scientific Computing – LNCC, Petrópolis, Brazil*
[d] *Rio de Janeiro State University – UERJ, Rio de Janeiro, Brazil*

Abstract

Asymmetries in bistable energy harvesters — arising from manufacturing tolerances, assembly misalignments, or operational conditions — are traditionally viewed as detrimental to performance. This study challenges that assumption through a comprehensive experimental investigation, demonstrating that controlled asymmetries can, under specific conditions, enhance energy harvesting. A prototype system was tested with asymmetry introduced via magnet rotation and shaker base tilting. We explored a wide range of configurations, excitation levels, and initial conditions. Results show that rotating the magnet weakens the magnetic attraction, shifting the resonance frequency downward. While base tilting utilizes gravitational effects to modify the magnetic interaction, further reducing its strength. Although pronounced asymmetries reduce power output at higher frequencies, they can significantly improve performance at lower frequencies, depending on system dynamics and excitation. Monostable and chaotic responses were also characterized numerically and experimentally. Overall, the findings reveal that asymmetry, when properly controlled, is not a flaw but a tunable design parameter to optimize bistable energy harvester performance.

Keywords: nonlinear dynamics, energy harvesting, piezoelectric vibration harvester, asymmetry effects, experimental nonlinear analysis

*Corresponding author

1. Introduction

Energy harvesting technologies aim to convert ambient energy—such as solar, wind, heat, and mechanical vibrations—into usable electrical power. Among these, vibration energy harvesting (VEH) has gained considerable attention due to its ubiquity across scales, from microelectromechanical systems (MEMS/NEMS) to large structures like vehicles and aircraft [1, 2, 3, 4, 5]. In many environments where solar and wind energy are inaccessible, pervasive vibrations transform wasted mechanical energy into a promising resource for low-power applications, including wireless sensor networks, embedded systems, and portable electronics [6, 7]. Among available transduction mechanisms—electrostatic, electromagnetic, and piezoelectric—piezoelectric energy harvesting (PEH) stands out for its higher energy density, simplicity, and scalability [2, 5, 8].

Over the last two decades, cantilevered piezoelectric coupled beams have emerged as the standard VEH architecture, enabling a variety of designs and applications. However, conventional linear PEH devices exhibit efficient energy conversion only near their natural frequency, thereby limiting their operational bandwidth. To broaden the frequency range, researchers have explored multi-degree-of-freedom systems [9, 10], multimodal designs [11, 12], adaptive tuning mechanisms [13, 14], and metamaterials [15, 16].

Nonlinear approaches, particularly bistable systems, have emerged as a robust solution to these bandwidth limitations by enabling enhanced energy capture under broadband or random excitations. Pioneering work demonstrated that magnetic coupling can induce bistability and significantly increase power output compared to linear designs [17, 18, 19]. Since then, a variety of nonlinear mechanisms have been investigated—including monostable, bistable, and multistable architectures [20, 21, 22, 23, 24], nonlinear piezoelectric coupling [25, 26, 27], and nonlinear damping effects [28, 29, 30]—further enriched by advanced models [31, 32, 33, 34, 35].

Despite these advances, nonlinear VEH systems inherently exhibit complex dynamics such as multi-stability, chaotic behavior, and strong sensitivity to initial conditions [36, 37]. Analytical studies have revealed intricate bifurcation phenomena [38], coexistence of solutions [39, 40], and significant dependence on system parameters [41, 42]. Moreover, nonlinear responses under various excitation types—parametric [43, 44], galloping [45, 46], and random [47, 48]—have been extensively analyzed.

Among the factors influencing performance, asymmetry is often unavoidable in practical bistable energy harvesters. Arising from manufacturing imperfections (e.g., magnet misalignments, beam deformation), assembly inaccuracies, or operational effects (e.g., gravitational bias, bolt loosening, environmental variability) [49, 50], asymmetry has historically been viewed as detrimental. However, recent theoretical and numerical studies indicate that controlled asymmetry can modify system dynamics and, under certain conditions, enhance performance [51, 52, 53]. For example, Wang et al. [51] explored multiple solutions in asymmetric systems under harmonic excitation, while Cao et al. [54] investigated the influence of time-varying potentials linked to asymmetry in human motion. Further, the role of bias angle adjustments on output power has been demonstrated in [55, 56], and our own numerical work confirmed that careful asymmetry compensation can restore symmetric-like behavior [57, 58, 59].

Despite these promising findings, experimental investigations of asymmetry effects remain limited. Prior studies have generally focused on isolated asymmetry sources, such as magnet mismatch, and have not addressed the complex interplay of multiple asymmetries—namely, magnet positioning and structural inclination—that commonly occur in real-world applications [51, 56, 60].

This work addresses this gap by presenting a comprehensive experimental study of a bistable energy harvester subjected to combined asymmetries from magnet rotation and base inclination. We systematically characterize the system's nonlinear dynamics, power output, and dynamic responses—including both monostable and chaotic regimes—across a wide range of configurations and excitation levels. Our findings reveal that, contrary to conventional assumptions, controlled asymmetry can be strategically exploited to enhance performance, particularly at low excitation levels where traditional designs are limited.

The paper is structured as follows: Section 2 presents the mathematical modeling and numerical characterization of the system. Section 3 details the experimental apparatus and testing methodology. Section 4 discusses the experimental results and dynamic behavior analysis. Finally, Section 5 summarizes the main conclusions and outlines potential future research directions.

2. Numerical exploration of the asymmetric dynamics

In this section, we introduce the mathematical formulation of the piezoelectric bistable energy harvester under both symmetric and asymmetric conditions and then present a detailed numerical exploration of its dynamic behavior. We begin with an overview of the dynamics of the system to establish the underlying physical principles, followed by numerical simulations that reveal the influence of asymmetry on the response of the system.

2.1. Mathematical modeling of the dynamical system

The classic piezoelectric bistable energy harvesting system consists of a rigid base supporting a vertical cantilever ferromagnetic beam with a fixed-free configuration. Two permanent magnets, symmetrically positioned near the lower part of the base, generate a nonlinear restoring force, resulting in two stable equilibrium points (potential wells) and one unstable equilibrium point. When the energy of the system exceeds the potential barrier, it undergoes interwell motion (snap-through behavior); otherwise, it remains in intrawell (monostable) motion.

In the upper section of the beam, where deformation is highest, a pair of piezoelectric layers is bonded and clamped. These layers are connected to a resistive circuit, converting kinetic energy into electrical energy, which is then dissipated through the resistor. An illustration of this system is shown in Fig. 1A.

The dimensionless lumped equations for the symmetric bistable energy harvester under harmonic excitation are given by [19]

$$\ddot{x} + 2\xi\dot{x} - \frac{1}{2}x(1-x^2) - \chi v = f\cos(\Omega t) \tag{1}$$

$$\dot{v} + \lambda v + \kappa\dot{x} = 0, \tag{2}$$

where ξ is the damping ratio, χ and κ are the piezoelectric coupling coefficients in the mechanical and electrical equations respectively, $\lambda \propto 1/(R_l C_p)$ is a reciprocal time constant, f is the forcing amplitude, and Ω is the excitation frequency. The initial conditions $(x_0, \dot{x}_0, v_0)$ represent the initial displacement, velocity, and voltage of the system.

The mean power generated is calculated as

$$P = \frac{1}{T}\int_{t_0}^{t_0+T} \lambda v(t)^2 \, \mathrm{d}t, \tag{3}$$

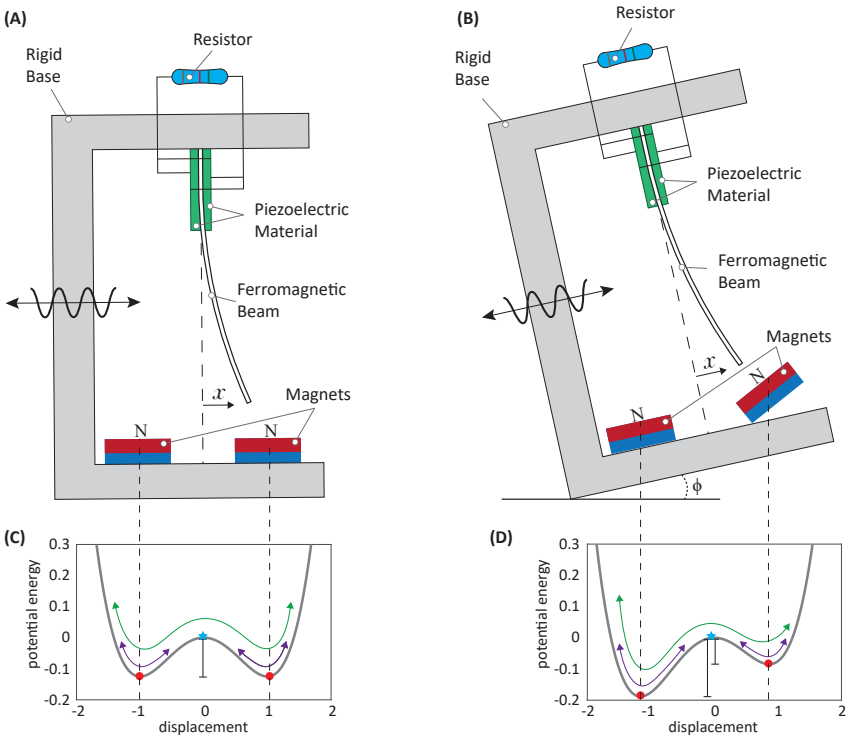

Figure 1: Schematic illustration of (A) symmetric and (B) asymmetric bistable energy harvesting systems. (C) Potential energy of the symmetric system with identical wells. (D) Potential energy of the asymmetric system, where the left well is deeper due to magnet misalignment and base tilting. Red circles indicate stable equilibrium points and blue stars indicate the unstable equilibrium point.

which represents the temporal average of the instantaneous power $\lambda v(t)^2$ over a period T [61].

Achieving a perfectly symmetric system in practice is challenging. To capture realistic asymmetries, additional terms are introduced. In particular, a quadratic nonlinearity with coefficient δ is added to model magnet misalignment [62, 49], and an external gravitational force term proportional to $p\sin(\phi)$ accounts for the effect of base tilting (with ϕ being the tilting angle) as illustrated in Fig. 1B. This extended model bridges the gap between idealized symmetry and real-world asymmetry:

$$\ddot{x} + 2\xi\dot{x} - \frac{1}{2}x(1 + 2\delta x - x^2) - \chi v = f\cos(\Omega t) + p\sin(\phi) \tag{4}$$

$$\dot{v} + \lambda v + \kappa \dot{x} = 0. \tag{5}$$

where δ quantifies the quadratic nonlinearity arising from magnet positioning, and p represents the equivalent dimensionless gravitational acceleration due to the base tilt. Nondimensionalization of the equations ensures that simulation results are comparable across different asymmetry configurations.

The nonlinear restoring force of the asymmetric bistable system is defined as

$$F_{nl}(x) = -\frac{1}{2}x(1 + 2\delta x - x^2) - p\sin(\phi). \tag{6}$$

Setting $F_{nl}(x) = 0$ yields three equilibrium points (one unstable, two stable). Figures 1C and D illustrate the potential energy for symmetric and asymmetric cases, respectively. In the asymmetric case, differences in the depth of the potential wells—affected by both magnet positioning and base tilting—lead to distinct energy barriers for transitions between equilibria.

2.2. Numerical characterization of the dynamics

The equations of motion [Eqs. (1)–(5)] are integrated numerically using a fourth-order Runge–Kutta method with a relative tolerance of 10^{-6} and an absolute tolerance of 10^{-9}. Simulations are conducted over a sufficiently long time span with a high sampling resolution to capture transient and steady-state behaviors. The simulation parameters are set to $\xi = 0.01$, $\chi = 0.05$, $\lambda = 0.05$, $\kappa = 0.5$, and $p = 0.59$, while Ω, f, ϕ, and δ are varied to explore a wide range of operating conditions. Initial conditions are selected based on the stable equilibria of Eq. (6), i.e., $(x_0, \dot{x}_0, v_0) = (\bar{x}_{1,2}, 0, 0)$, ensuring that the simulations accurately reflect the response of the system near these points.

Figure 2 presents phase portraits for various configurations under low, medium, and high excitation levels. In Fig. 2A, the symmetric system ($\delta = 0$, $\phi = 0°$) exhibits intrawell motion at low excitation, transitions to chaotic behavior at medium levels (evidenced by a strange attractor), and eventually shows periodic interwell motion at high excitation. Figures 2B–D illustrate the dynamics of asymmetric systems. For example, in Fig. 2B, with $\delta = 0.15$ and $\phi = 10°$, the right potential well is deeper, resulting in lower oscillation amplitudes near that well, while the left well exhibits higher amplitudes. Conversely, Fig. 2C (with $\delta = -0.15$, $\phi = 10°$) shows stronger attraction at the left, causing larger oscillations when initial conditions are near the right magnet. The trajectories (depicted in red, blue, and green) serve as indicators of intrawell, interwell, and invariant (initial condition–independent)

responses, respectively. Annotations on the figures further highlight these key dynamic features.

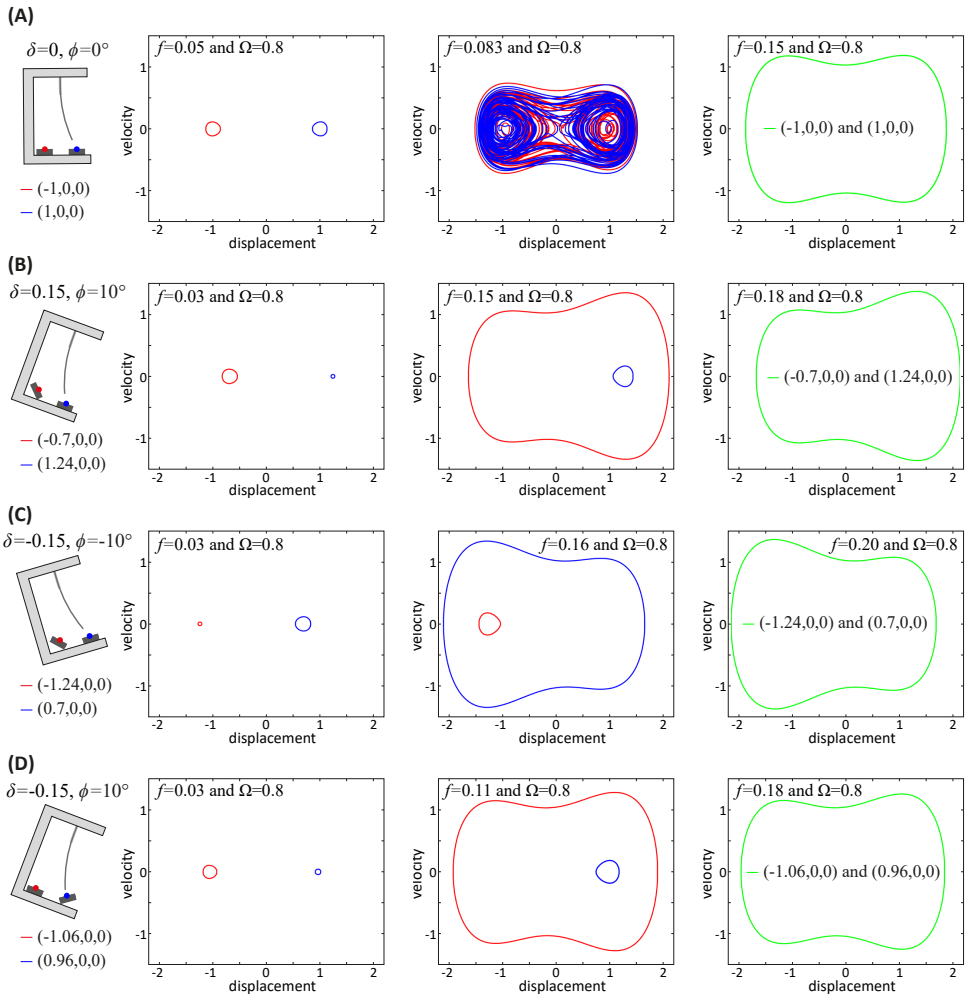

Figure 2: Numerical phase portraits for (A) the symmetric system and (B–D) asymmetric systems under low, medium, and high excitation levels. Red and blue lines represent trajectories initiated at the left and right stable equilibria, respectively, while the green line indicates trajectories that are independent of the initial condition.

Figure 3 illustrates the corresponding energy harvesting performance, with mean power computed according to Eq. (3). Notably, at high excitation levels the mean power converges across configurations; however, at intermediate levels the harvested energy varies significantly with initial conditions

and system asymmetry. This trend underscores the practical importance of controlling asymmetry to optimize power output.

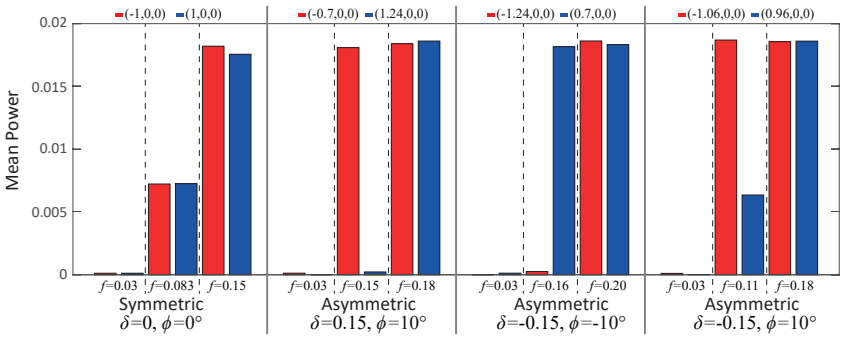

Figure 3: Mean output power of symmetric and asymmetric bistable energy harvesters for the configurations in Fig. 2. Dashed lines separate excitation regimes, and different colors indicate distinct initial conditions.

For a more detailed dynamic analysis, including basins of attraction and bifurcation diagrams, we refer the reader to our previous work [57].

3. Experimental apparatus and testing methodology

This section details the experimental setup used to investigate asymmetry in a bistable energy harvester. We describe the prototype design, instrumentation, and testing protocols that enable controlled evaluation under both symmetric and asymmetric conditions.

3.1. Prototype description

To explore the effects of asymmetry, we fabricated a test prototype illustrated in Fig. 4 consisting of four major components:

I *Supporting Structure:* A lightweight aluminum frame, assembled in two parts, provides a rigid base that permits both linear translation and adjustable rotation.

II *Clamping Device:* Ensures a secure attachment of the piezoelectric coupled beam with zero deflection, emulating a clamped boundary condition at the end.

III *Instrumented Piezoelectric Beam:* A spring steel beam (dimensions: 145 $\times$ 25.4 $\times$ 0.25 mm^3) is equipped with piezoelectric sensors (MIDÉ qp16n) bonded on both surfaces using high-shear epoxy adhesive (3M DP460N). The piezoelectric patches are connected in parallel to a load resistor with resistance $R_L = 10^6\,\Omega$, approximating an open-circuit condition. Two rigid steel lumped masses are symmetrically attached at the free end to reduce the natural frequency of the piezoelectric coupled beam and enhance magnetic interaction.

IV *Rotatable Neodymium Magnets:* Two cylindrical permanent magnets, housed in 3D-printed adjustable holders, provide a attractive magnetic force with the steel masses. This magnetoelastic interaction generates a nonlinear restoring force, establishing a stable equilibrium point at each magnet. The magnet holder positions (both linear and angular) can be independently altered to create symmetric or asymmetric configurations.

Figures 4A-B show the system under symmetric conditions (magnet holders and shaker oriented horizontally), while Figs. 4C-E illustrate various asymmetric configurations, achieved by rotating the left magnet holder (C), rotating the shaker base (D), or both (E).

3.2. Instrumentation and signal flow

The entire assembly is mounted on an electromagnetic shaker (TIRA Vib Modal Exciter S 51110-M) with an adjustable base. Three measurement modalities are used:

- *Acceleration Measurement:* An ICP® miniature accelerometer (PCB model 352A24, 98 mV/g, 0.5 g) is attached to the base to record acceleration.

- *Voltage Measurement:* The voltage across the load resistor, generated by the bimorph piezoelectric layers, is monitored to capture the electrical output.

- *Velocity Measurement:* A single-point laser vibrometer (Polytec OFV-505) measures the absolute velocity at a point near the beam tip. A reflective tape is applied to enhance the signal-to-noise ratio; the vibrometer is mounted on a tripod to maintain proper orientation even when the base is rotated.

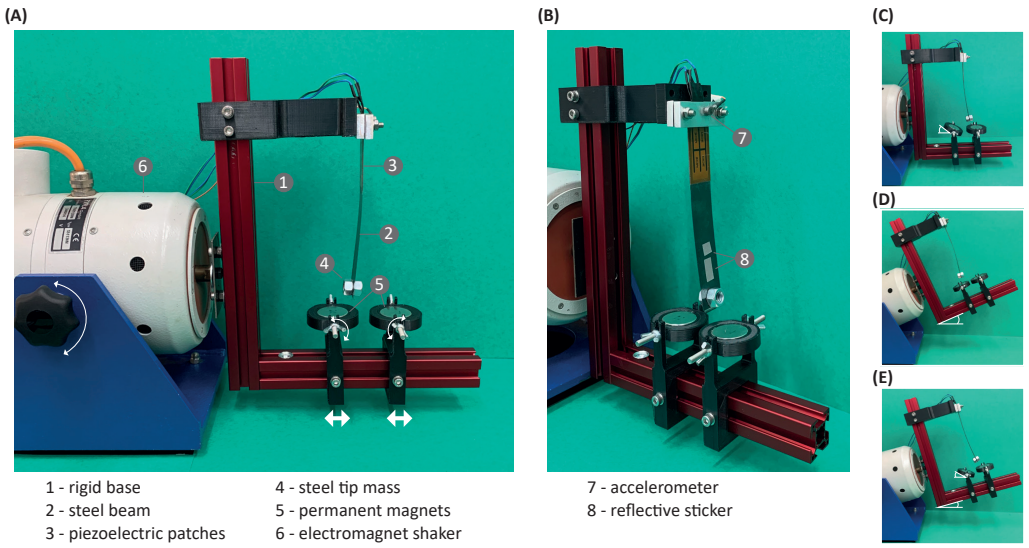

Figure 4: Experimental setup of the bistable energy harvester. (A) Photo of the system mounted on an electromagnetic shaker, showing the linear translation and rotation capabilities of the magnet holders and base. (B) Diagonal view of the system, with numbered components. (C-E) Photos of the system under different asymmetric configurations: (C) left magnet rotated, (D) base rotated, and (E) both left magnet and base rotated.

Figure 5 presents the signal flow diagram. The DAQ system (LMS SCADAS Mobile) generates the excitation signal (fed to a TIRA BAA 500 power amplifier and then to the shaker) and simultaneously acquires data from the accelerometer, voltage sensor (using 10× attenuation probes), and vibrometer (after signal conditioning through the Polytec OFV-5000 control unit). The base acceleration is introduced to the DAQ's reference channel via ICP coupling. The DAQ is interfaced with a computer running LMS Testlab software.

3.3. Excitation protocols and data acquisition

3.3.1. Swept sine excitation tests

Swept sine is applied over the $0-20$ Hz range. Tests are performed with 1600 spectral lines, providing a frequency resolution of $\Delta f = 15.625$ mHz and a time interval of $\Delta T = 15.625$ ms over an analysis period of $T = 64$ s. A low input voltage ($V_i = 5$ mV) is used to avoid snap-through motion. Hanning windows are applied to reduce digital filter leakage, following standard practices [63]. These tests primarily determine the fundamental natural frequencies at both bistable positions and offer preliminary insights into the asymmetry-induced nonlinear restoring forces.

The base drive transmissibility tests are conducted on the test prototype to measure the electromechanical voltage transmissibility by comparing the output voltage to the input acceleration in the frequency domain. Purely systemic viewpoint, this expression is given by

$$\alpha(\omega) = \frac{V_o(\omega)}{A_i(\omega)}, \tag{7}$$

where $\alpha(\omega)$ is the voltage FRF, $A_i(\omega)$ stands for the input base acceleration and $V_o(\omega)$ stands for the output voltage. The quantities in Equation 7 are in the frequency domain, representing the Fourier transforms of their time-domain variables [63]. In this work, the FRF is estimated using motion transmissibility calculated from single side auto and cross-spectrum densities $G_{ii}(\omega)$ and $G_{io}(\omega)$, as defined in Equation 8 (see [63] for details).

$$H_1(\omega) = \frac{G_{io}(\omega)}{G_{ii}(\omega)}. \tag{8}$$

3.3.2. Single-frequency excitation tests

For nonlinear systems with multiple coexisting responses, single-frequency tests provide a clearer picture of the dynamic behavior. The system is excited

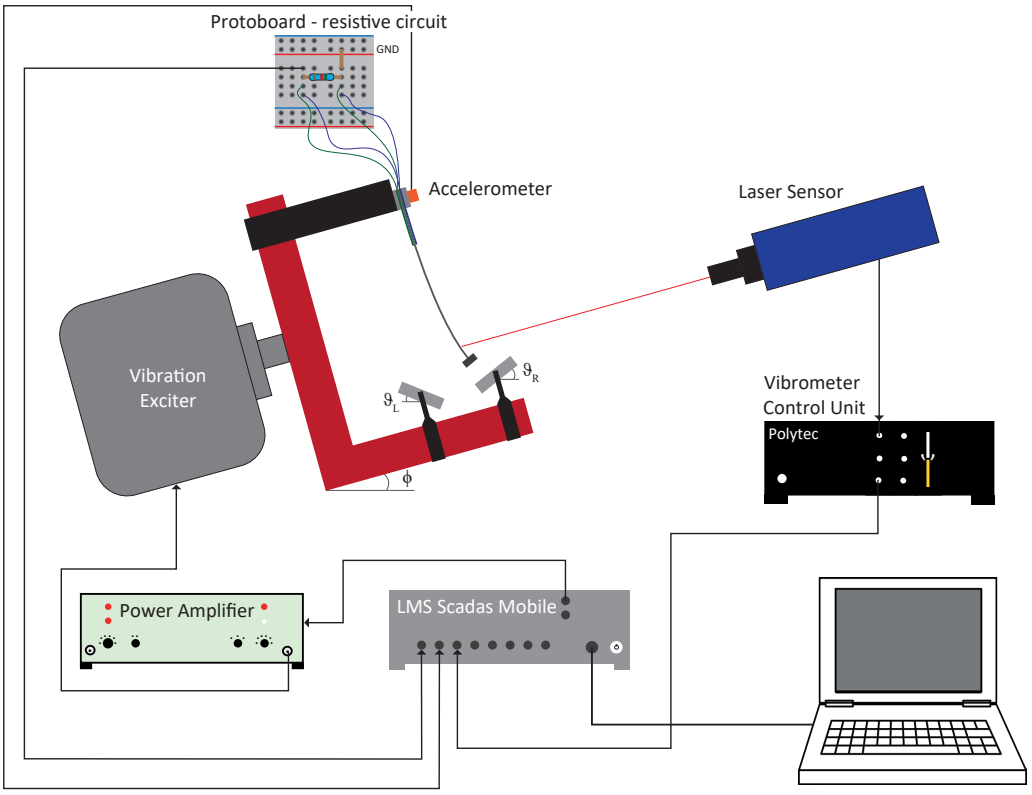

Figure 5: Schematic diagram of the experimental setup and signal flow for the bistable energy harvesting system. The diagram details the excitation signal generated by the DAQ and amplified by the TIRA BAA 500, which drives the electromagnetic shaker. Simultaneously, the system measures the base acceleration via an ICP accelerometer, the voltage output from the piezoelectric bimorph (across a $10^6\,\Omega$ load resistor) using $10\times$ attenuation probes, and the beam tip velocity using a laser vibrometer. The signal conditioning modules and data acquisition through the LMS Testlab software are also depicted.

at various frequencies and amplitudes (ranging from low to high) to capture regular and irregular motions. To accurately capture superharmonic frequencies, the time resolution is improved to $\Delta T = 7.8125$ ms. The measured velocity is integrated in the frequency domain to reconstruct its displacement trajectory. Additionally, Poincaré maps—constructed using a stroboscopic approach with the excitation frequency—are used to visualize the global nonlinear dynamics [37].

4. Results and discussion

The experimental results are analyzed in two main parts. First, we examine the frequency response of the system under swept sine excitation to assess changes in natural frequency and damping due to asymmetry. Second, we analyze the power output and state-space dynamics under single-frequency excitation to correlate dynamic behavior with energy harvesting performance.

4.1. Frequency response under swept sine excitation

Swept sine excitation tests were conducted using a low input voltage (5 mV) to confine the beam's motion to intrawell oscillations. Figure 6 shows the Frequency Response Function (FRF) for various system configurations, with red curves representing oscillations around the left equilibrium and blue curves corresponding to the right equilibrium.

In the symmetric configuration ($\phi = \vartheta_L = \vartheta_R = 0°$; Fig. 6A), the natural frequencies at the two equilibria are nearly identical, confirming that the restoring forces are balanced. In contrast, when only one magnet is rotated, the natural frequency shifts noticeably. For example, Fig. 6B (with $\vartheta_R = 30°$) shows a lower natural frequency for the right equilibrium, while Fig. 6C (with $\vartheta_L = 30°$) shows a similar shift for the left equilibrium. These shifts are attributed to the reduction in magnetic attraction caused by increased magnet-to-beam distances.

When the base is rotated (Fig. 6D; $\phi = 45°$ with $\vartheta_L = \vartheta_R = 0°$), the FRF indicates that the natural frequency is higher for the left than for the right equilibrium points, due to the influence of the gravitational component. In configurations combining base and magnet rotation (Figs. 6E-F), the interplay of gravitational and magnetic effects becomes evident: while the left magnet rotation (Fig. 6E) shifts the natural frequency downward, a compensatory effect is observed when the right magnet is rotated (Fig. 6F), where the frequencies nearly converge to symmetric values. Table 1 summarizes

the natural frequencies for all cases, highlighting the quantitative impact of asymmetry on system dynamics.

The FRF also provides critical insights into energy harvesting efficiency, as its amplitude reflects the damping characteristics of the system. Generally, lower and wider peaks indicate higher damping, which results in greater energy dissipation, reduced oscillation amplitude, and thus, lower energy conversion. For the symmetric configuration (Fig.6B-F), the FRF exhibits peaks of varying amplitudes, with higher peaks corresponding to the magnet with weaker attraction. This observation suggests that asymmetry influences the effective distribution of damping, leading to different rates of energy dissipation and ultimately affecting overall energy harvesting performance.

Case	Natural frequency (Hz)	
	Left position	Right position
(A) $\phi = 0^\circ$, $\vartheta_L = 0^\circ$, $\vartheta_R = 0^\circ$	9.21	9.18
(B) $\phi = 0^\circ$, $\vartheta_L = 0^\circ$, $\vartheta_R = 30^\circ$	7.00	9.60
(C) $\phi = 0^\circ$, $\vartheta_L = 30^\circ$, $\vartheta_R = 0^\circ$	7.54	9.18
(D) $\phi = 45^\circ$, $\vartheta_L = 0^\circ$, $\vartheta_R = 0^\circ$	7.97	7.25
(E) $\phi = 25^\circ$, $\vartheta_L = 30^\circ$, $\vartheta_R = 0^\circ$	4.64	8.42
(F) $\phi = 25^\circ$, $\vartheta_L = 0^\circ$, $\vartheta_R = 60^\circ$	8.12	7.76

Table 1: Natural frequency of the responses presented for the left and the right position for each case shown in Fig. 6.

Summary: These FRF measurements demonstrate that asymmetry—introduced either via magnet rotation or base tilting—can significantly alter the natural frequency and, by inference, the energy dissipation characteristics of the harvester.

4.2. Power output and state-space analysis under single-frequency excitation

In addition to swept sine excitation tests, single-frequency experiments were performed to investigate the power harvesting performance and dynamic behavior in both intrawell and interwell (chaotic) regimes.

4.2.1. Power output analysis

Two excitation frequencies were selected: 9.1 Hz, which aligns with the natural frequency of the symmetric system, and 6.3 Hz, which approximates

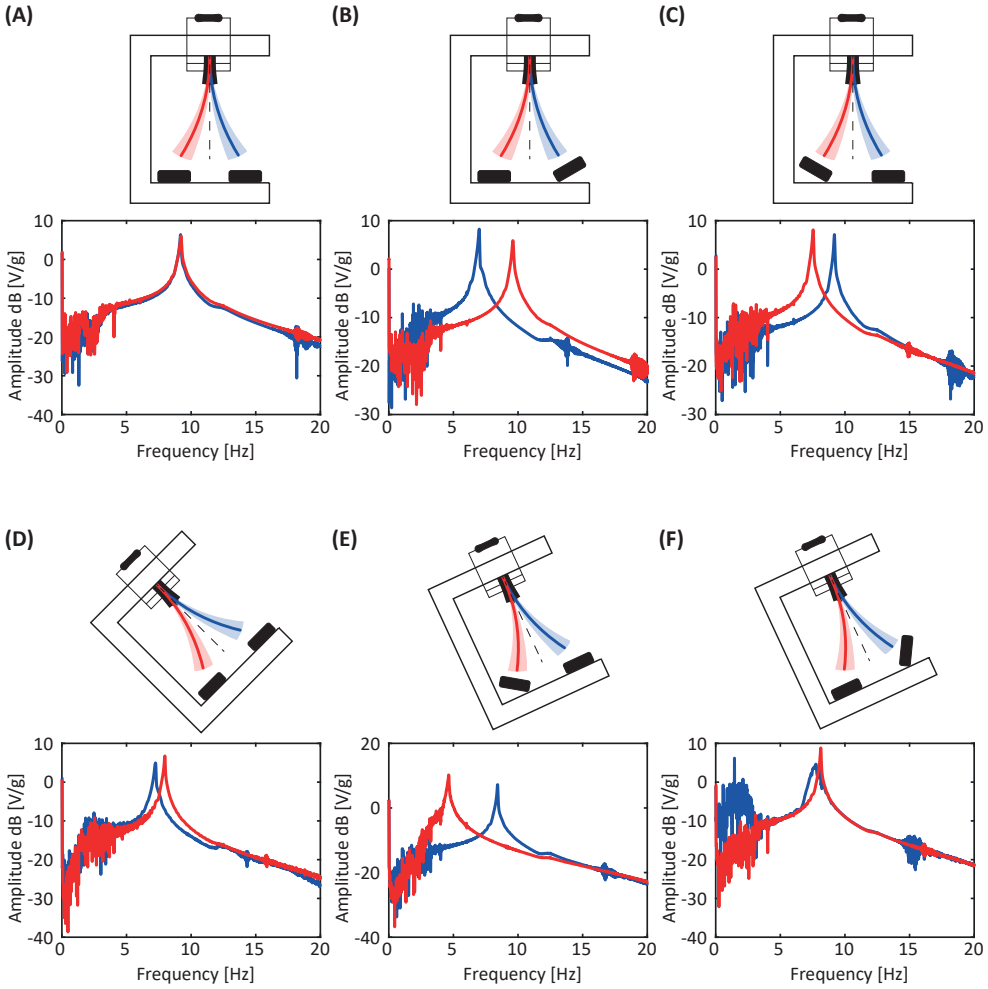

Figure 6: Frequency responses of the bistable energy harvester under a 5 mV input voltage excitation for various configurations. (A) Symmetric ($\phi = \vartheta_L = \vartheta_R = 0°$), (B) Asymmetric ($\phi = \vartheta_L = 0°$, $\vartheta_R = 30°$), (C) Asymmetric ($\phi = \vartheta_R = 0°$, $\vartheta_L = 30°$), (D) Asymmetric ($\phi = 45°$, $\vartheta_L = \vartheta_R = 0°$), (E) Asymmetric ($\phi = 25°$, $\vartheta_L = 30°$, $\vartheta_R = 0°$), (F) Asymmetric ($\phi = 25°$, $\vartheta_L = 0°$, $\vartheta_R = 60°$). Red curves represent the response about the left equilibrium, while blue curves represent the response about the right equilibrium.

the frequency of resonances observed in asymmetric cases. The average power output is calculated using

$$P_{avg} = \frac{V_{rms}^2}{R_L}, \tag{9}$$

where V_{rms} is the root mean square voltage and R_L is the load resistance.

Figures 7–10 summarize the average power outputs under different base rotation angles and magnet configurations. For instance, when the base rotation is null ($\phi = 0°$, Fig. 7), the asymmetric configuration with left magnet rotation yields higher power at 6.3 Hz, while at 9.1 Hz, the configuration with right magnet rotation performs better. As the base rotation increases (10°, 25°, and 45°), the energy harvesting performance varies, revealing that both excitation frequency and the interplay of magnet and base rotations critically affect power output. Notably, lower natural frequencies favor power generation at 6.3 Hz, whereas higher natural frequencies favor 9.1 Hz excitation.

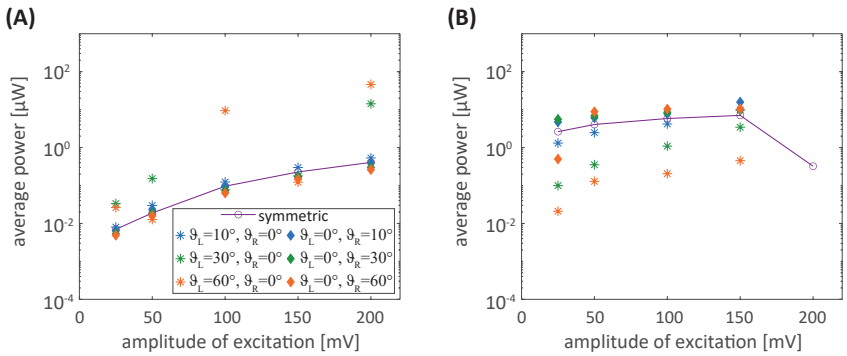

Figure 7: Average power output of the bistable energy harvester for various magnet configurations at $\phi = 0°$ under excitation frequencies of (A) 6.3 Hz and (B) 9.1 Hz.

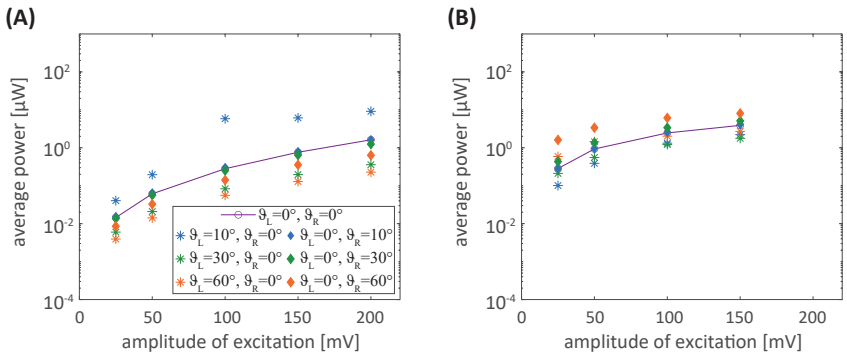

Figure 8: Average power output for various magnet configurations when the base is rotated by $\phi = 10°$ under excitation frequencies of (A) 6.3 Hz and (B) 9.1 Hz.

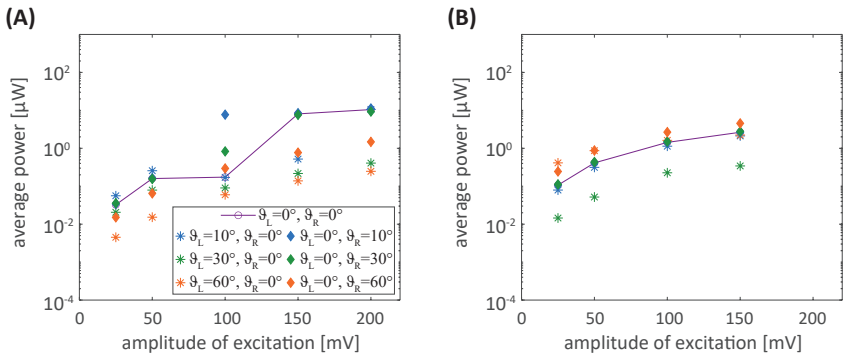

Figure 9: Average power output for various magnet configurations when the base is rotated by $\phi = 25°$ under excitation frequencies of (A) 6.3 Hz and (B) 9.1 Hz.

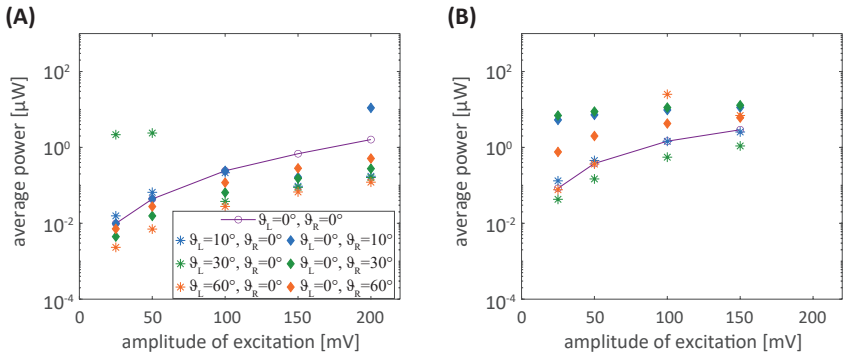

Figure 10: Average power output for various magnet configurations when the base is rotated by $\phi = 45°$ excitation frequencies of (A) 6.3 Hz and (B) 9.1 Hz.

Figure 11 presents the average power output for different base rotation angles without magnet rotation. The results clearly show that the asymmetric configuration outperforms the symmetric one at 6.3 Hz. However, at 9.1 Hz, the symmetric configuration yields the highest power output across all excitation amplitudes.

Summary: The power output varies with excitation frequency and asymmetry configuration. In many cases, asymmetric configurations outperform the symmetric case, although the optimal setup depends on the specific frequency and excitation amplitude.

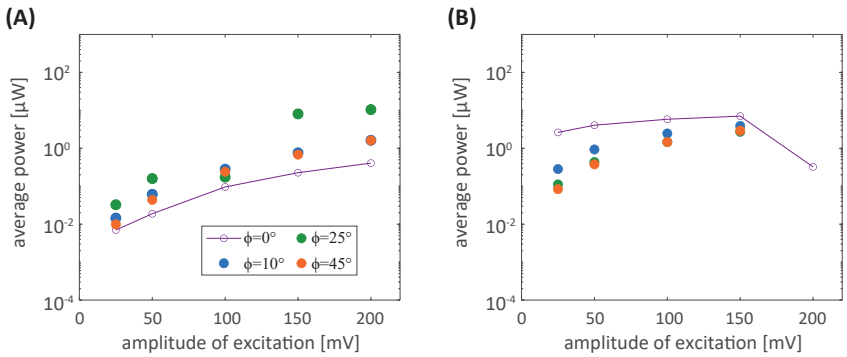

Figure 11: Average power output for various base rotation angles (with no magnet rotation) under excitation frequencies of (A) 6.3 Hz and (B) 9.1 Hz. The symmetric system (with $\phi = 0°$) is used as a reference.

4.2.2. State-space and Poincaré analysis

The state-space analysis further investigates the dynamic of the system by reconstructing its trajectory (displacement vs. velocity) from the measured velocity and estimated displacement (obtained via frequency-domain integration) and by computing the corresponding Poincaré maps. The orbit size provides insight into energy harvesting efficiency: larger orbits indicate higher displacement and greater energy conversion, while smaller orbits suggest lower displacement and reduced energy harvesting. Numerical results, based on the governing equations in Eqs. 4 and 5, provide a qualitative comparison with experiments.

The motion of the system is first analyzed in the monostable regime under a 50 mV excitation at 6.3 Hz. Video S1 (electronic supplementary material) illustrates its experimental response for different configurations. To ensure numerical consistency, parameters are set to observe an equivalent response from the experimental tests. For the symmetric configuration ($\vartheta_L = 0°$, $\vartheta_R = 0°$, and $\phi = 0°$), the equivalent numerical parameters are $\xi = 0.01$, $\chi = 0.05$, $\lambda = 0.05$, $\kappa = 0.5$, $p = 0.59$, $\delta = 0$ and $\phi = 0°$, with excitation parameters $f = 0.05$ and $\Omega = 0.8$ ensuring a monostable regime. For the asymmetric configuration ($\vartheta_L = 30°$, $\vartheta_R = 0°$ and $\phi = 25°$), the equivalent numerical parameters are adjusted to $\delta = 0.70$ and $\phi = 25°$, while excitation remains $f = 0.05$ and $\Omega = 0.8$. The initial conditions of the numerical results are defined with zero initial velocity and voltage, while the initial displacement is set at each stable equilibrium point.

In Figure 12, the top panels (A and C) show experimental results in dimensional units, while the bottom panels (B and D) present numerical simulations in dimensionless form. Panels A and B correspond to the symmetric configuration, and panels C and D correspond to the asymmetric configuration. Although a direct quantitative comparison is not possible due to the different scales, the qualitative behavior is remarkably similar. The experimental results (Fig. 12A) display a period-one orbit with superimposed Poincaré points, confirming a stable response. A slight difference in energy between the left and right orbits in the experimental data hints at minor unintentional asymmetries.

For the asymmetric configuration, the experimental results (Fig. 12C) show that the orbit around one equilibrium (typically the left) contains more energy than the other. This observation aligns with the FRF results and underscores the significant influence of controlled asymmetry on the system's dynamics.

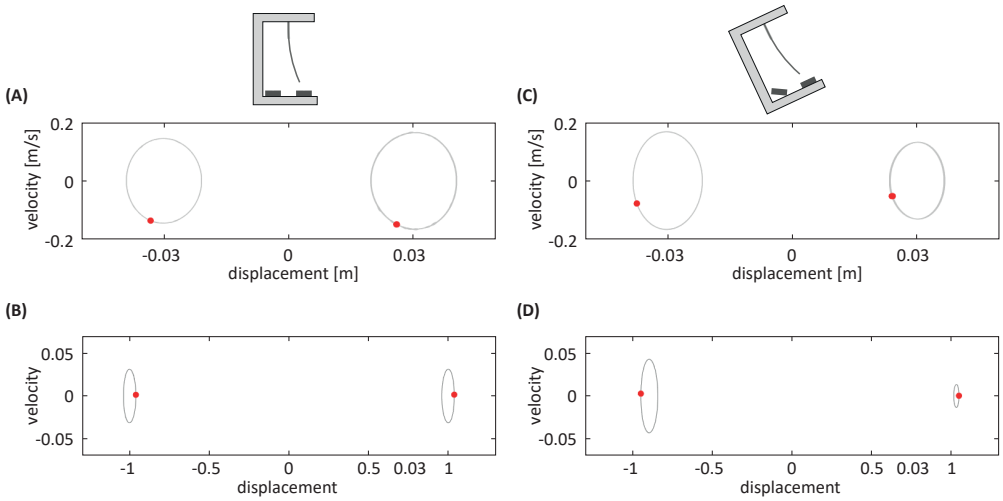

Figure 12: Phase portraits and Poincaré maps in the monostable regime for symmetric (left column) and asymmetric (right column) configurations. Red points denote the Poincaré map. Negative displacement orbits correspond to the left equilibrium, while positive ones correspond to the right equilibrium. (A) and (C) present experimental results; (B) and (D) show numerical simulations.

Next, the excitation parameters are adjusted to induce chaotic motion using the same configurations from Fig. 12. Experimentally, chaos occurs at 6.5 Hz with 150 mV for the symmetric case and 172 mV for the asymmetric

case (see Video S2). Numerically, it is observed at $f = 0.083$ and $\Omega = 0.8$ for the symmetric case and $f = 0.26$ and $\Omega = 0.5$ for the asymmetric case, with initial conditions set at a stable equilibrium point.

Figure 13 similarly shows experimental results (top panels) and numerical simulations (bottom panels). Both sets of results reveal complex interwell motions and fractal Poincaré maps. In the symmetric case, numerical results display perfectly symmetric orbits, while experimental data show slight asymmetry, likely due to system imperfections, as previously discussed. In the asymmetric case, the experimental and numerical maps consistently indicate that the orbit around the right equilibrium is larger, reflecting a deeper potential well and a higher energy requirement for interwell transitions.

The numerical Poincaré map contains more points due to the shorter experimental time series, but the fractal pattern remains visible. Additionally, chaotic motion in numerical results emerged only at higher excitation levels, producing larger attractors than in the symmetric case. Despite the lack of model calibration, the qualitative agreement provides insights into system dynamics and the role of magnetic attraction in asymmetry modeling.

4.2.3. Energy harvesting performance

Figure 14 summarizes the experimental average power under both intrawell (monostable) and chaotic regimes. In the intrawell regime, the symmetric system shows nearly equal power at both equilibria, whereas the asymmetric system displays significant disparity, with higher power output from the equilibrium where the system retains more energy. In chaotic motion, both systems produce higher power; however, the asymmetric system generally yields superior performance.

Overall Summary: The results indicate that the dynamic response and energy harvesting performance of the bistable system are strongly influenced by asymmetry. While symmetric configurations offer balanced behavior, appropriate asymmetry (through magnet and base rotation) can enhance power output under specific excitation conditions, albeit with greater sensitivity to initial conditions and nonlinear effects.

5. Final remarks

This paper presents an in-depth experimental analysis of a bistable energy harvesting system, demonstrating how controlled asymmetries—introduced via magnet rotation and shaker base tilting—affect both its dynamic behavior

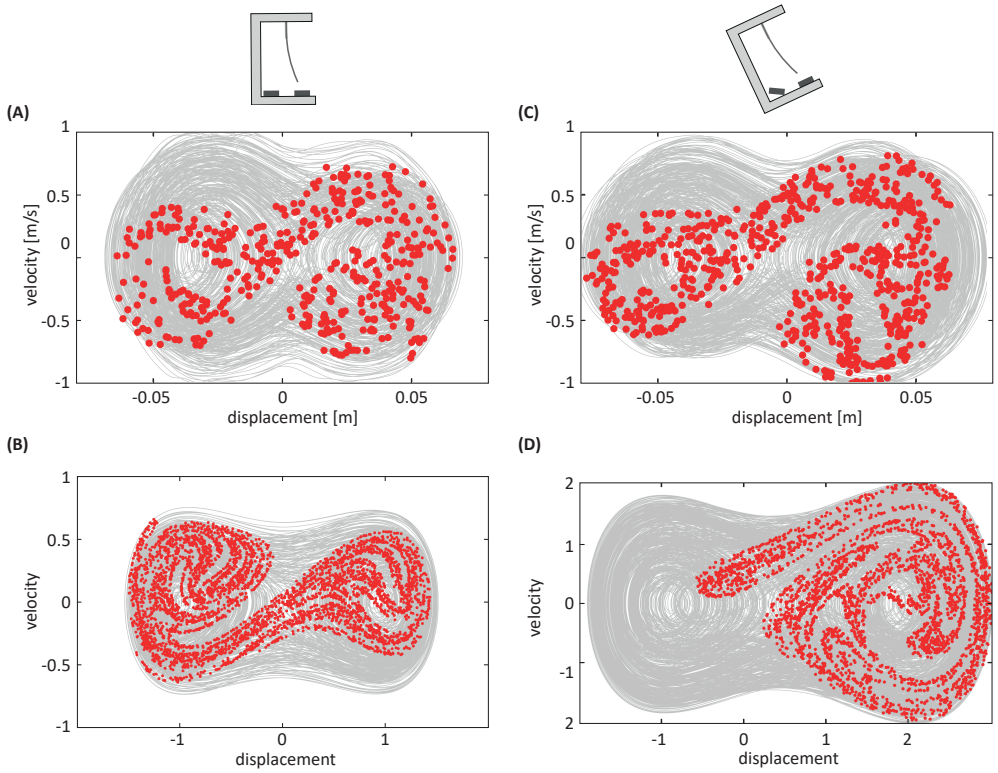

Figure 13: Phase portraits and Poincaré maps under chaotic motion for (A-B) symmetric and (C-D) asymmetric configurations. The maps reveal a fractal structure with multiple intersecting trajectories, confirming chaotic dynamics.

and energy conversion performance. A custom-designed prototype was tested under symmetric and various asymmetric conditions, and its performance was characterized across different initial conditions and excitation intensities.

Frequency-domain analysis under swept sine excitation revealed that asymmetry alters the natural frequency of the system. Specifically, rotating the magnets reduces the restoring force by increasing the distance between the magnet and the beam, thereby lowering the natural frequency at the corresponding equilibrium point. The base rotation (e.g., anticlockwise tilt) reduces the beam's attraction to the right equilibrium point, effectively shifting its natural frequency downward. These findings indicate that the precise configuration of magnet and base rotations can be tuned to modulate the asymmetry intensity, although these relationships depend on prototype-specific parameters such as magnet dimensions and positioning.

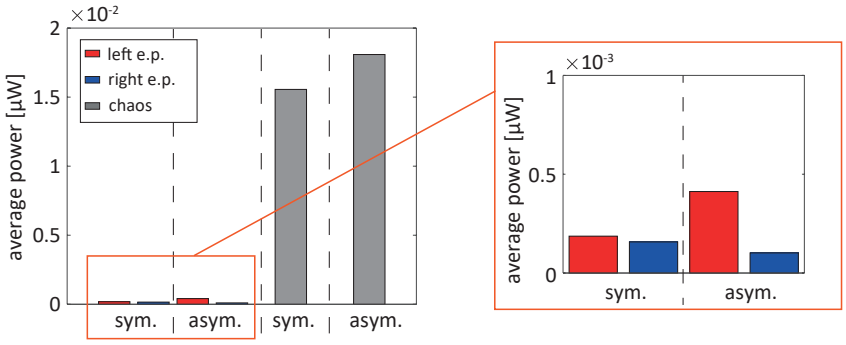

Figure 14: Experimental average power for symmetric and asymmetric configurations. Red bars represent power when oscillating around the left equilibrium, blue bars for the right equilibrium, and gray bars for chaotic motion.

Time-domain experiments under single-frequency excitation further demonstrated that asymmetric configurations can outperform the symmetric system under certain conditions. In many cases, asymmetric configurations yield higher power output at lower excitation frequencies, while strong asymmetry—especially with a high base tilt—can result in reduced power at higher frequencies. Moreover, state-space trajectories and Poincaré maps reveal that imposed asymmetries significantly influence the system's oscillatory behavior, affecting both stability and energy distribution across equilibrium points.

In summary, our experimental study provides critical insights into the dynamic behavior and energy harvesting performance of bistable systems under asymmetrical conditions. The results suggest that, while symmetric designs offer balanced responses, intentionally engineered asymmetry can serve as a powerful design parameter to optimize energy harvesting performance in nonlinear systems. These findings pave the way for future research aimed at exploiting controlled asymmetries to enhance the efficiency of practical energy harvesting devices.

Acknowledgments

The authors gratefully acknowledge the fruitful discussions on this work with Prof. Domingos Alves Rade (ITA, Brazil).

Funding

This research received financial support from the National Council for Scientific and Technological Development (CNPq) under grants 309467/2023-3 and 305476/2022-0; the Coordination for the Improvement of Higher Education Personnel (CAPES) - Finance Code 001; the Carlos Chagas Filho Research Foundation of Rio de Janeiro State (FAPERJ) under grants 210.167/2019 and 204.477/2024; and the INCT-EIE (National Institute of Science and Technology - Smart Structures in Engineering), funded by CNPq under grant number 406148/2022-8, as well as FAPEMIG (Minas Gerais State Research Support Foundation).

Declaration of interests

The authors declare that they have no known competing financial interests or personal relationships that could have appeared to influence the work reported in this paper.

Supplementary data

Movie S1: Vibration Test of a Bistable Energy Harvester under Monostable Motion (Symmetric and Asymmetric Configurations). This video demonstrates intrawell oscillations of the bistable energy harvester when excited at a single frequency and amplitude. Both symmetric and various asymmetric configurations are tested, highlighting the differences in dynamic response under monostable conditions.

Movie S2: Vibration Test of a Bistable Energy Harvester under Chaotic Motion (Symmetric and Asymmetric Configurations). This video captures the chaotic oscillatory behavior of the bistable energy harvester under single-frequency excitation. The tests, performed for both symmetric and asymmetric configurations, illustrate the complex dynamics and the influence of asymmetry on system performance.

Data availability

The data used in this study are available at the GitHub repository **BistableX: Bistable eXploration in Energy Harvesting**, which can be accessed at `https://americocunhajr.github.io/BistableX`.

Disclaimer

This manuscript was rigorously revised for grammatical clarity and language quality using AI-powered tools such as Grammarly and ChatGPT. Nonetheless, the authors assume full responsibility for the original language and phrasing.

References

[1] F. K. Shaikh, S. Zeadally, Energy harvesting in wireless sensor networks: A comprehensive review, Renewable and Sustainable Energy Reviews 55 (2016) 1041–1054. doi:10.1016/j.rser.2015.11.010.

[2] H. Liu, J. Zhong, C. Lee, S.-W. Lee, L. Lin, A comprehensive review on piezoelectric energy harvesting technology: Materials, mechanisms, and applications, Applied Physics Reviews 5 (4) (2018) 041306. doi:10.1063/1.5074184.

[3] C. Chen, T.-B. Xu, A. Yazdani, J.-Q. Sun, A high density piezoelectric energy harvesting device from highway traffic — system design and road test, Applied Energy 299 (2021) 117331. doi:10.1016/j.apenergy.2021.117331.

[4] S. Panda, S. Hajra, K. Mistewicz, P. In-na, M. Sahu, P. M. Rajaitha, H. J. Kim, Piezoelectric energy harvesting systems for biomedical applications, Nano Energy 100 (2022) 107514. doi:10.1016/j.nanoen.2022.107514.

[5] T. Li, P. S. Lee, Piezoelectric energy harvesting technology: From materials, structures, to applications, Small Structures 3 (3) (2022) 2100128. doi:10.1002/sstr.202100128.

[6] Y. Zou, V. Raveendran, J. Chen, Wearable triboelectric nanogenerators for biomechanical energy harvesting, Nano Energy 77 (2020) 105303. doi:10.1016/j.nanoen.2020.105303.

[7] X. Wang, Y. Zhang, X. Zhang, Z. Huo, X. Li, M. Que, Z. Peng, H. Wang, C. Pan, A highly stretchable transparent self-powered triboelectric tactile sensor with metallized nanofibers for wearable electronics, Advanced Materials 30 (12) (2018) 1706738. doi:10.1002/adma.201706738.

[8] A. Erturk, D. Inman, Piezoelectric Energy Harvesting, Wiley, New York, 2011.

[9] I. Kim, H. Jung, B. Lee, S. Jang, Broadband energy-harvesting using a two degree-of-freedom vibrating body, Applied Physics Letters 98 (2011) 1. doi:10.1063/1.3595278.

[10] H. Xiao, X. Wang, S. John, A multi-degree of freedom piezoelectric vibration energy harvester with piezoelectric elements inserted between two nearby oscillators, Mechanical Systems and Signal Processing 68 (2016) 138. doi:10.1016/j.ymssp.2015.07.001.

[11] V. Caetano, M. Savi, Multimodal pizza-shaped piezoelectric vibration-based energy harvesters, Journal of Intelligent Material Systems and Structuresdoi:10.1177/1045389X211006910.

[12] X. Li, K. Yu, D. Upadrashta, Y. Yang, Multi-branch sandwich piezoelectric energy harvester: mathematical modeling and validation, Smart Materials and Structures 28 (2019) 035010. doi:10.1088/1361-665X/aaf8bf.

[13] D.-G. Lee, J. Shin, H. S. Kim, S. Hur, S. Sun, J.-S. Jang, S. Chang, I. Jung, S. Nahm, H. Kang, C.-Y. Kang, S. Kim, J. M. Baik, I.-R. Yoo, K.-H. Cho, H.-C. Song, Autonomous resonance-tuning mechanism for environmental adaptive energy harvesting, Advanced Science 10 (3) (2023) 2205179. doi:10.1002/advs.202205179.

[14] S. Ibrahim, W. Ali, A review on frequency tuning methods for piezoelectric energy harvesting systems, Journal of Renewable and Sustainable Energy 4 (2012) 062703. doi:10.1063/1.4766892.

[15] T. Tan, Z. Yan, K. M. H. Zou, F. Liu, L. Zhao, Z. Peng, W. Z, Renewable energy harvesting and absorbing via multi-scale metamaterial systems for internet of things, Applied Energy 254 (2019) 113717. doi:10.1016/j.apenergy.2019.113717.

[16] Z. Chen, B. Guo, Y. Yang, C. Cheng, Metamaterials-based enhanced energy harvesting: A review, Physica B: Condensed Matter 438 (2014) 1–8. doi:10.1016/j.physb.2013.12.040.

[17] F. Cottone, H. Vocca, L. Gammaitoni, Nonlinear energy harvesting, Physical Review Letters 102 (2009) 080601. doi:10.1103/PhysRevLett.102.080601.

[18] L. Gammaitoni, I. Neri, H. Vocca, Nonlinear oscillators for vibration energy harvesting, Applied Physics Letters 94. doi:10.1063/1.3120279.

[19] A. Erturk, J. Hoffmann, D. Inman, A piezomagnetoelastic structure for broadband vibration energy harvesting, Applied Physics Letters 94 (2009) 254102. doi:10.1063/1.3159815.

[20] K. Fan, Q. Tan, Y. Zhang, S. Liu, M. Cai, Y. Zhu, A monostable piezoelectric energy harvester for broadband low-level excitations, Applied Physics Letters 112 (12) (2018) 123901. doi:10.1063/1.5022599.

[21] K. Fan, Q. Tan, H. Liu, Y. Zhang, M. Cai, Improved energy harvesting from low-frequency small vibrations through a monostable piezoelectric energy harvester, Mechanical Systems and Signal Processing 117 (2019) 594–608. doi:10.1016/j.ymssp.2018.08.001.

[22] R. Naseer, A. Abdelkefi, Nonlinear modeling and efficacy of viv-based energy harvesters: Monostable and bistable designs, Mechanical Systems and Signal Processing 169 (2022) 108775. doi:10.1016/j.ymssp.2021.108775.

[23] Q. Liu, W. Qin, Y. Yang, Z. Zhou, Harvesting weak vibration energy by amplified inertial force and multi-stable buckling piezoelectric structure, Mechanical Systems and Signal Processing 189 (2023) 110125. doi:10.1016/j.ymssp.2023.110125.

[24] A. Mitura, M. Brunetti, L. Kloda, F. Romeo, J. Warminski, Experimental nonlinear dynamic regimes for energy harvesting from cantilever bistable shells, Mechanical Systems and Signal Processing 206 (2024) 110890. doi:10.1016/j.ymssp.2023.110890.

[25] A. Triplett, D. Quinn, The effect of nonlinear piezoelectric coupling on vibration-based energy harvesting, Journal of Intelligent Material Systems and Structures 20 (2009) 1959–1967. doi:10.1177/1045389X09343218.

[26] B. M. S. Stanton, A. Erturk, D. Inman, Nonlinear piezoelectricity in electroelastic energy harvesters: Modeling and experimental identification, Journal of Applied Physics 108 (2010) 074903. doi:10.1063/1.3486519.

[27] S. Leadenham, A. Erturk, Unified nonlinear electroelastic dynamics of a bimorph piezoelectric cantilever for energy harvesting, sensing, and actuation, Nonlinear Dynamics 79 (2015) 1727–1743. doi:10.1007/s11071-014-1770-x.

[28] S. Z. D. Huang, R. Li, G. Litak, Theoretical analysis of vibration energy harvesters with nonlinear damping and nonlinear stiffness, The European Physical Journal Plus 133 (510). doi:10.1140/epjp/i2018-12298-0.

[29] S. P. Machado, M. Febbo, C. D. Gatti, S. M. Osinaga, A piezoelectric beam model with geometric, material and damping nonlinearities for energy harvesting, Smart Materials and Structures 29 (9) (2020) 095009. doi:10.1088/1361-665X/ab9ddb.

[30] Y. Zhu, Z. Lang, Beneficial effects of antisymmetric nonlinear damping with application to energy harvesting and vibration isolation under general inputs, Nonlinear Dynamics 108 (2022) 2917–2933. doi:10.1007/s11071-022-07444-0.

[31] H. O. Y. Fu, R. Davis, Nonlinear dynamics and triboelectric energy harvesting from a three-degree-of-freedom vibro-impact oscillator, Nonlinear Dynamics 92 (2018) 1985–2004. doi:10.1007/s11071-018-4176-3.

[32] S. Leadenham, A. Erturk, Mechanically and electrically nonlinear non-ideal piezoelectric energy harvesting framework with experimental validations, Nonlinear Dynamics 99 (2020) 625–641. doi:10.1007/s11071-019-05091-6.

[33] A. Adeodato, B. T. Duarte, L. L. S. Monteiro, P. M. C. Pacheco, M. A. Savi, Synergistic use of piezoelectric and shape memory alloy elements for vibration-based energy harvesting, International Journal of Mechanical Sciences 194 (2021) 106206. doi:10.1016/j.ijmecsci.2020.106206.

[34] J. Margielewicz, D. Gaska, G. Litak, P. Wolszczak, D. Yurchenko, Nonlinear dynamics of a new energy harvesting system with quasi-zero stiffness, Applied Energy 307 (2022) 118159. doi:10.1016/j.apenergy.2021.118159.

[35] J. P. Norenberg, A. Cunha Jr, P. Wolszczak, G. Litak, Piezomagnetic vibration energy harvester with an amplifier, Theoretical and Applied Mechanics Letters 13 (2023) 100478. doi:10.1016/j.taml.2023.100478.

[36] M. Daqaq, R. Masana, A. Erturk, D. Quinn, On the role of nonlinearities in vibratory energy harvesting: A critical review and discussion, Applied Mechanics Reviews 66 (2014) 040801. doi:10.1115/1.4026278.

[37] S. H. Strogatz, Nonlinear Dynamics and Chaos: with applications to Physics, Biology, Chemistry, and Engineering, Vol. 2, Westview Press, Boulder, 2014.

[38] P. Kim, J. Seok, A multi-stable energy harvester: Dynamic modeling and bifurcation analysis, Journal of Sound and Vibration 333 (21) (2014) 5525–5547. doi:10.1016/j.jsv.2014.05.054.

[39] G. Litak, J. Margielewicz, D. Gaska, P. Wolszczak, S. Zhou, Multiple solutions of the tristable energy harvester, Energies 14 (5). doi:10.3390/en14051284.

[40] V. G. Lopes, J. V. L. L. Peterson, A. Cunha Jr, Nonlinear characterization of a bistable energy harvester dynamical system, in: M. Belhaq (Ed.), Topics in Nonlinear Mechanics and Physics, Springer, Singapore, 2019. doi:10.1007/978-981-13-9463-8_3.

[41] L. G. Costa, L. L. da Silva Monteiro, P. M. C. L. Pacheco, M. A. Savi, A parametric analysis of the nonlinear dynamics of bistable vibration-based piezoelectric energy harvesters, Journal of Intelligent Material Systems and Structures 32 (7) (2021) 699–723. doi:10.1177/1045389X20963188.

[42] T. Tan, Z. Yan, K. Ma, F. Liu, L. Zhao, W. Zhang, Nonlinear characterization and performance optimization for broadband bistable energy harvester, Acta Mechanica Sinica 36 (2020) 578–591. doi:10.1007/s10409-020-00946-3.

[43] G. X. F. Fang, J. Wang, Nonlinear dynamic analysis of cantilevered piezoelectric energy harvesters under simultaneous parametric and external excitations, Acta Mechanica Sinica 34 (2018) 561–577. doi:10.1007/s10409-017-0743-y.

[44] Y. Fan, M.-Q. Niu, M. H. Ghayesh, M. Amabili, L.-Q. Chen, Nonlinear vibration energy harvesting via parametric excitation: Snap-through with time-varying potential wells, Mechanical Systems and Signal Processing 220 (2024) 111625. doi:10.1016/j.ymssp.2024.111625.

[45] Z. Yan, A. Abdelkefi, Nonlinear characterization of concurrent energy harvesting from galloping and base excitations, Nonlinear Dynamics 77 (2014) 1171–1189. doi:10.1007/s11071-014-1369-2.

[46] J. Wang, H. Xiang, Y. Ci, X. Xue, Exploring the effect of incoming wind turbulent flow on galloping-based piezoelectric energy harvesting, Mechanical Systems and Signal Processing 221 (2024) 111714. doi:10.1016/j.ymssp.2024.111714.

[47] G. Litak, M. I. Friswell, S. Adhikari, Magnetopiezoelastic energy harvesting driven by random excitations, Applied Physics Letters 96 (21) (2010) 214103. doi:10.1063/1.3436553.

[48] M. Bakhtiari-Shahri, H. Moeenfard, Energy harvesting from unimorph piezoelectric circular plates under random acoustic and base acceleration excitations, Mechanical Systems and Signal Processing 130 (2019) 502–523. doi:10.1016/j.ymssp.2019.05.017.

[49] E. Halvorsen, Fundamental issues in nonlinear wideband-vibration energy harvesting, Phys. Rev. E 87 (2013) 042129. doi:10.1103/PhysRevE.87.042129.

[50] H. Qifan, M. Daqaq, Influence of potential function asymmetries on the performance of nonlinear energy harvesters under white noise, Journal of Sound and Vibration 333 (15) (2014) 3479–3489. doi:10.1016/j.jsv.2014.03.034.

[51] C. B. W. Wang, J. Cao, G. Litak, Multiple solutions of asymmetric potential bistable energy harvesters: numerical simulation and experimental validation, Eur Phys J B 91. doi:10.1140/epjb/e2018-90180-y.

[52] C. B. W. Wang, J. Cao, G. Litak, Probability and output analysis of asymmetric bistable energy harvesters subjected to gaussian white noise, Eur Phys J Plus 134. doi:10.1140/epjp/i2019-13080-6.

[53] X. Ma, H. Li, S. Zhou, Z. Yang, G. Litak, Characterizing nonlinear characteristics of asymmetric tristable energy harvesters, Mechanical Systems and Signal Processing 168 (2022) 108612. doi:10.1016/j.ymssp.2021.108612.

[54] J. Cao, W. Wang, S. Zhou, D. Inman, J. Lin, Probability and output analysis of asymmetric bistable energy harvesters subjected to gaussian white noise, Applied Physics Letters 107. doi:10.1140/epjp/i2019-13080-6.

[55] D. I. W. Wang, J. Cao, J. Lin, Performance enhancement of nonlinear asymmetric bistable energy harvesting from harmonic, random and human motion excitations, Applied Physics Letters 112 (2018) 213903. doi:10.1063/1.5027555.

[56] W. Wang, J. Cao, C. Bowen, Y. Zhang, J. Lin, Nonlinear dynamics and performance enhancement of asymmetric potential bistable energy harvesters, Nonlinear Dynamics 94 (2018) 1183–1194. doi:10.1007/s11071-018-4417-5.

[57] J. Norenberg, R. Luo, V. Lopes, J. Peterson, A. Cunha, Nonlinear dynamics of asymmetric bistable energy harvesters, International Journal of Mechanical Sciences 257 (2023) 108542. doi:10.1016/j.ijmecsci.2023.108542.

[58] J. Norenberg, A. Cunha Jr., S. da Silva, P. Varoto, Global sensitivity analysis of asymmetric energy harvesters, Nonlinear Dynamics 109 (2022) 443–458. doi:10.1007/s11071-022-07563-8.

[59] J. P. Norenberg, A. Cunha Jr, S. da Silva, P. S. Varoto, Probabilistic maps on bistable energy harvesters, Nonlinear Dynamics 111 (2023) 20821–20840. doi:10.1007/s11071-023-08864-2.

[60] Q. Li, L. Bu, S. Lu, B. Yao, Q. Huang, X. Wang, Practical asymmetry and its effects on power and bandwidth performance in bi-stable vibration energy harvesters, Mechanical Systems and Signal Processing 206 (2024) 110939. doi:10.1016/j.ymssp.2023.110939.

[61] A. Cunha Jr, Enhancing the performance of a bistable energy harvesting device via the cross-entropy method, Nonlinear Dynamics 103 (2021) 137–155. doi:10.1007/s11071-020-06109-0.

[62] J. Cao, W. Wang, S. Zhou, D. Inman, J. Lin, Nonlinear time-varying potential bistable energy harvesting from human motion, Applied Physics Letters 107 (2015) 143904. doi:10.1063/1.4932947.

[63] K. McConnell, P. Varoto, Vibration Testing: Theory and Practice, Vol. 2, Wiley, New York, 2008.